APPLIED PHYSICS

Chip-scale atomic wave-meter enabled by machine learning

Eitan Edrei[1], Niv Cohen[2], Elam Gerstel[1], Shani Gamzu-Letova[1], Noa Mazurski[1], Uriel Levy[1]*

The quest for miniaturized optical wave-meters and spectrometers has accelerated the design of novel approaches in the field. Particularly, random spectrometers (RS) using the one-to-one correlation between the wavelength and an output random interference pattern emerged as a promising tool combining high spectral resolution and cost-effectiveness. Recently, a chip-scale platform for RS has been demonstrated with a markedly reduced footprint. Yet, despite the evident advantages of such modalities, they are very susceptible to environmental fluctuations and require an external calibration process. To address these challenges, we demonstrate a paradigm shift in the field, enabled by the integration of atomic vapor with a photonic chip and the use of a machine learning classification algorithm. Our approach provides a random wave-meter on chip device with accurate calibration and enhanced robustness against environmental fluctuations. The demonstrated device is expected to pave the way toward fully integrated spectrometers advancing the field of silicon photonics.

INTRODUCTION

Spectral analysis is a metrological measure that is highly essential for diverse fields of study, ranging from photonics and atomic physics to materials science and biochemical sensing, to name a few. Typically, grating-based spectrometers are used to provide the spectral signature of either an interrogated light source or any transmission or reflection response of a sample. However, the spectral resolving power (i.e., spectral resolution) of such grating-based devices is typically limited to ~0.1 nm for a footprint of 1 cm (1). For many applications such as Brillouin spectroscopy, laser frequency stabilization or the study of atomic spectroscopic lines, such resolution, is far from being sufficient, and a much higher spectral resolution is required (2–9). To accommodate the need for high spectral resolution, advanced spectrometers based on interferometric effects such as Fabry-Perot virtually imaged phased array (VIPA) or Michelson interferometers were developed and are nowadays commercially available. The ultrahigh spectral resolution (<1 pm) provided by such instruments comes with an unavoidable downside, e.g., high-cost, meter-sized footprint and, oftentimes, a lengthy scanning procedure.

In recent years, a new and exciting class of spectrometers/wave-meters named "random spectrometers" (RS) has emerged as a promising tool for spectral analysis (10). The underlying principle of RS is that as light propagates through a random scattering medium, each wavelength generates a unique light pattern, which can be identified via a precalibration process. Beyond cost and size considerations, the advantage of RS is the broadband operating range and the lack of redundancy set by the free spectral range of conventional spectrometers. In this context, different platforms have been suggested as a scattering medium; reflections from rough surfaces via free space propagation have been demonstrated with a footprint of tens of centimeters (11). Alternatively, the mode interference pattern within very long multimode fibers has been used to encode the spectral information (12, 13). All these configurations are still inferior in terms of size parameters; furthermore, they are very sensitive to jitters of the system.

On-chip RS devices pose the advantage of being cost-effective and compact. Yet, size reduction trades off with spectral resolution as the wavelength-dependent decorrelation of the transmitted pattern scales inversely with the device physical dimensions. Such compact device has been demonstrated, yet with a relatively low spectral resolution of ~0.5 nm (14). To improve the spectral resolution and enable high-end measurements using chip-scale devices, a spiral platform with extended length of light propagation has been used (1), and indeed, an improved spectral resolution of up to 0.01 nm has been demonstrated using such spiral platform fabricated in silicon and combined with evanescence enhancement as well as appropriate reconstruction algorithms. Despite the promising opportunities enabled by such portable cost-effective precise device, the chip-scale RS platform is strongly susceptible to environmental modifications, particularly temperature fluctuations (15). In addition, as in other spectrometers, it requires an external calibrated source for the calibration process.

To provide the needed paradigm shift in the field, we hereby bring together three advanced disciplines, namely, chip-scale integrated photonics, chip-scale atomic vapors, and machine learning algorithms. In particular, we show that by integrating a spiral multimode waveguide with a rubidium vapor that is directly interacting with the guided mode and using a suitable machine learning algorithm, a robust spectrometer device that is both accurately calibrated and provides a better immunity toward environmental fluctuations can be realized. Our modality presents a crucial step in paving the way toward the integration of high-end spectrometers within silicon photonic–based systems. Such devices will hopefully become suitable for broad commercialization and will contribute to myriad scientific and technological applications relying on miniaturized yet precise and robust spectroscopic devices.

RESULTS

The operational principle of our device is presented in Fig. 1. A tunable laser source is coupled into a silicon nitride multimode spiral waveguide via a grating coupler port (Fig. 1A). The multimode waveguide is

[1]Department of Applied Physics, The Center for Nanoscience and Nanotechnology, The Hebrew University, Jerusalem 91904, Israel. [2]School of Computer Science and Engineering, The Hebrew University, Jerusalem 91904, Israel.
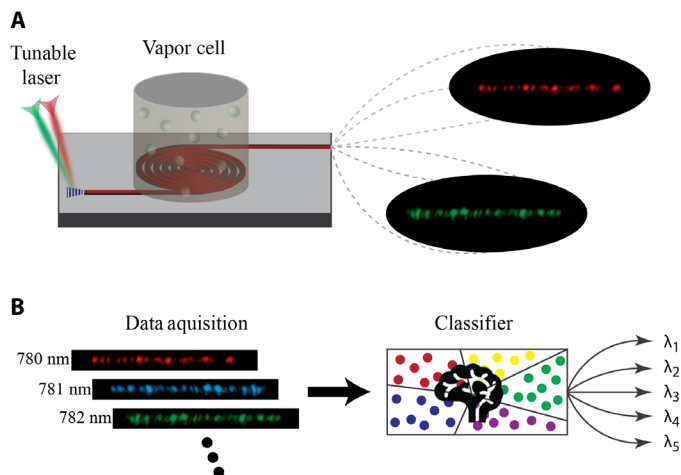*Corresponding author. Email: ulevy@mail.huji.ac.il

Fig. 1. Operation principle. (**A**) Schematic description of the operation principle. Light from a tunable laser is coupled into the device, and the output image for each wavelength is recorded by a CMOS camera as the laser is scanned. (**B**) All outputs are fed into a classifier to generate the correlation map between each wavelength and the corresponding pattern.

50 μm wide and 250 nm thick. In such a configuration, each mode is partially localized to the silicon nitride, while its evanescent field is decaying outside of the core and is thus interacting with the cladding medium. To take advantage of this very nature, the device is encapsulated within a rubidium (Rb) vapor cell to allow direct interactions between the atomic vapor and the evanescent field. The availability of the atomic vapor on a chip will later serve as an absolute reference for the wavelength measurements. The output light pattern is collected and imaged into a complementary metal oxide semiconductor (CMOS) sensor while scanning the input wavelength to generate a spatial transmission matrix, correlating each input wavelength to an output pattern. Next, all patterns are fed into a classification algorithm with the proper labels (i.e., matching wavelength) as shown in Fig. 1B to generate a multidimensional map for pattern-to-wavelength correlation.

A detailed scheme of the experimental setup is shown in Fig. 2A. First, the spiral waveguide device is fabricated (see Materials and Methods) and placed on a heating resistor to enable the control over the Rb vapor density when voltage is applied. To couple light into the grating coupler, an imaging system is constructed using a light-emitting diode (LED) for illumination (Thorlabs, M565L3) and a charge-coupled device (CCD) for image acquisition (C1, DCC1545M). The collimated LED emission is focused through a dichroic mirror onto the back aperture of the objective lens (O1, Olympus LMPLN-IR 10×) to illuminate a large region of the sample. Next, a collimated tunable laser (New Focus TLB-6700) is reflected off the dichroic mirror and directed by the same objective lens (O1) into the grating coupler with an angle of ~5°. The angle of incidence is set by tuning the laser incident location on the back aperture of the objective lens through lateral translation of the dichroic mirror. A second imaging system encompassing an objective lens (O2, Nikon Plan Fluor ELWD 20×), a tube lens and a CMOS camera (C2, Hamamatsu Orca-Flash 4.0) is situated at the output of the device to image the resulting pattern.

To quantify the spectral resolution of the system, we heated the vapor cell to ~100° and recorded the output while scanning the

wavelength. This process resulted in a series of patterns similar to those shown in Fig. 1B; by averaging each pattern and placing it as a column of a matrix, we constructed the transmission matrix of the system (Fig. 2B). The D_2 absorption lines of Rb 87 are marked with a white dashed line, and the region is enlarged in Fig. 2C. The spectral distance between the absorption lines corresponds to ~6.034 GHz, from which the spectral separation between two adjacent columns can be accurately extracted (see the Supplementary Materials). From the transmission matrix, it is straightforward to obtain the correlation function by taking the autocorrelation of Fig. 2B and plotting the central row (Fig. 2D). Fundamentally, the width of the correlation function determines the spectral resolution of the device (when the correct transmission matrix is available), as it represents the patterning decorrelation as the wavelength is detuned. In our case, we have measured a spectral resolution of ~0.013 nm at half width at half maximum for a spiral of ~27 cm long (for analysis of the spectral resolution dependency on spiral length, see the Supplementary Materials).

From a fundamental standpoint, the phase accumulated by a mode propagating through the device is given by $\varphi = \beta_n \times L$, where β_n is the propagation constant of mode number n, and L is the propagation length (the change in the propagation constant between the various modes is attributed to a difference in the effective-refractive index, which is governed by the mode confinement within the waveguide). The maximal phase difference occurs between the lowest and highest modes, i.e., (*13*)

$$\Delta\varphi \ = \ (\beta_1 - \beta_{max}) \cdot L \tag{1}$$

A substantial change in $\Delta\varphi$ will result in a noticeable variation of the resulting pattern; hence, by requiring a π phase shift, we can extract the wavelength shift $\delta\lambda$ for which the output pattern is significantly varied

$$\frac{d\Delta\varphi}{d\lambda} \cdot \delta\lambda \approx \pi \tag{2}$$

By substituting $\Delta\varphi$ from Eq. 1 into Eq. 2, we can express the spectral resolution $\delta\lambda$ as

$$\delta\lambda \approx \frac{\pi}{L} \cdot \left[\frac{d(\beta_1 - \beta_{max})}{d\lambda} \right]^{-1} \tag{3}$$

We calculated the derivative in Eq. 3 numerically as follows: The modes propagating through the waveguide were obtained using the a mode-solver simulation (Lumerical,;see the Supplementary Materials), from which the propagation constant values $\beta(\lambda)$ for the fundamental and the highest-order mode were extracted. The derivative in Eq. 3 is, by definition, the slope of the difference between $\beta_1(\lambda)$ and $\beta_{max}(\lambda)$. The spectral resolution obtained from this analytical argument considering the dimensions of our devices is $\delta\lambda \approx 5$ pm, which is better than the experimental results shown in Fig. 2D by threefold. The reason for the discrepancy between the analytical results and the experimental ones is that Eq. 1 assumes that there is no mode mixing throughout the process. However, in practice, mode mixing occurs, and therefore, the propagation constant of a mode that originally propagated with β_1 cannot be assumed to continue propagating with the same propagation constant. The propagation constant therefore needs to be calculated as

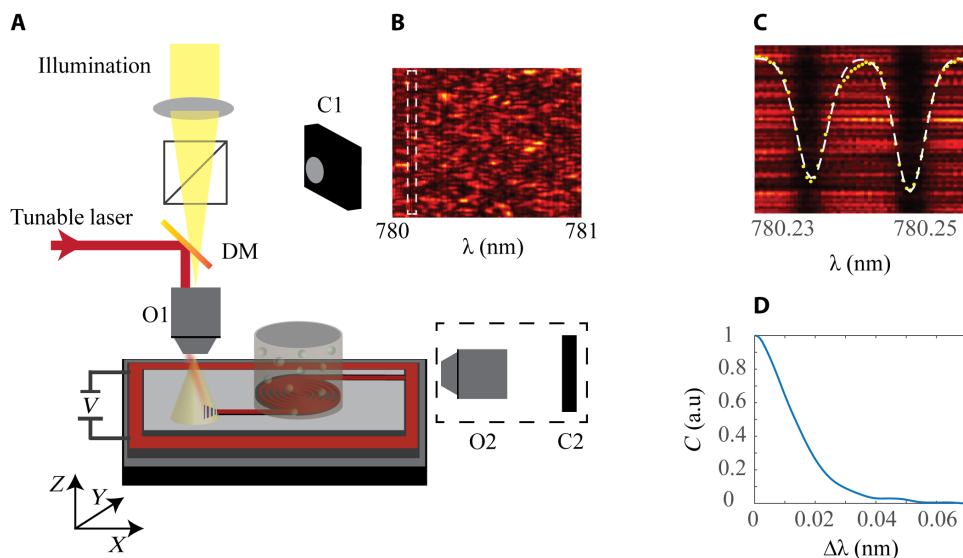**Fig. 2. Experimental setup and performances.** (**A**) Schematics of the full experimental setup. (**B**) Measured transmission matrix of the device. (**C**) Enlarged region of the dashed line in (B) showing the Rb absorption lines. (**D**) One-dimensional correlation function of the matrix shown in (B). a.u., arbitrary units.

a weighted average over all propagation constants of the different modes to which energy was transferred.

Next, we show the capability of retrieving the spectral signature of an unknown input from the given precalibration data. First, we demonstrate the performance of a truncated singular value decomposition (SVD) algorithm as outlined elsewhere (*13*); this algorithm calculates the pseudoinverse matrix of the measured transmission matrix and multiplies it by an unknown output pattern to retrieve the spectrum. To implement this method, we performed two wavelength scans through the spiral device. The first scan was used as a transmission matrix calibration, while inputs from the second scan where used as the test inputs for spectrum identification. Figure 3A shows the reconstructed spectrum of a single wavelength; red line represents the ground-truth input, while the reconstruction is shown as a blue line. The reconstruction is in good agreement with the ground truth, and the reconstruction width at full width at half maximum (FWHM) is ~0.02 nm, which agrees with the quantified spectral resolution obtained in Fig. 2D.

Another important measure of any spectrometer is the bandwidth of operation, which is dictated by the spectral resolution and the number of modes supported by the device: $B = N \times \delta\lambda$, where B is the bandwidth and N is the number of supported modes (*13*). We evaluated numerically the number of supported modes to be ~200; however, because only transverse electric (TE) polarized light was coupled into the device and some modes exhibit stronger losses than others, it cannot be assumed that all modes are excited and contribute equally to the performances. Instead, we estimated the number of contributing channels experimentally by evaluating the number of speckles present on the exit facet of the spiral waveguide. To do so, we calculated the autocorrelation of the transmission matrix (i.e., Fig. 2B) and measured the width of the central peak in the Y axis. Considering our spectral resolution of 25 pm (FWHM) and the 40 speckles visualized at the exit facet, the bandwidth of our device is ~1 nm. Figure 3B shows the reconstruction of a continuous spectrum with uniform light distribution of ~0.6 nm (blue) compared to the ground-truth spectrum (red).

The ability to reconstruct a continuous spectrum together with the integrated Rb cell configuration enables an absolute measurement (rather than a relative one) of a wavelength by measuring the distance to an absorption line. This can be simply implemented by injecting light from a relatively broad light source encompassing the Rb D_2 absorption lines together with the interrogated source. Figure 3C shows a reconstruction of single wavelength together with a continuous spectrum encompassing the region of the Rb absorption lines. The two absorption lines (black arrows) serve as an absolute fixed reference point to determine the wavelength of interest.

Sensitivity to thermal fluctuations can significantly affect the performances of our device. To quantify this parameter, we locked the incident laser (externally) to one of the Rb transition lines and acquired the outcoming pattern as the temperature was monotonically decreased. The maximal value of the cross correlation between the first pattern to all other patterns is plotted in Fig. 3D. As expected, correlation is degraded as the temperature drifts; we estimate a 50% correlation loss at $\Delta T \approx 0.5°$. An approximated value of ΔT can also be obtained analytically; the thermo-optical coefficient of silicon nitride is (*16*) $\frac{dn}{dT} \approx 2 \times 10^{-5}$, and the optical path difference accumulated through the device for two different temperatures is given by

$$\Delta\varphi = kL \cdot (n_{T1} - n_{T2}) = kL \cdot \frac{dn}{dT}\Delta T \qquad (4)$$

Because the modes propagating through the device are located partially in the surrounding vapor, we take the thermo-optical coefficient to be the average between air and silicon nitride, i.e., $\frac{dn}{dT} \approx 10^{-5}$. By requiring a π phase variation in Eq. 4 and substituting the parameters of our device, a temperature decorrelation value of $\Delta T \approx 0.15$ is obtained, which is in the same order of magnitude as the measured value.

Last, we address the issue of sensitivity to thermal fluctuations. When there is a considerable time difference between the construction of the transmission matrix and the wavelength measurement
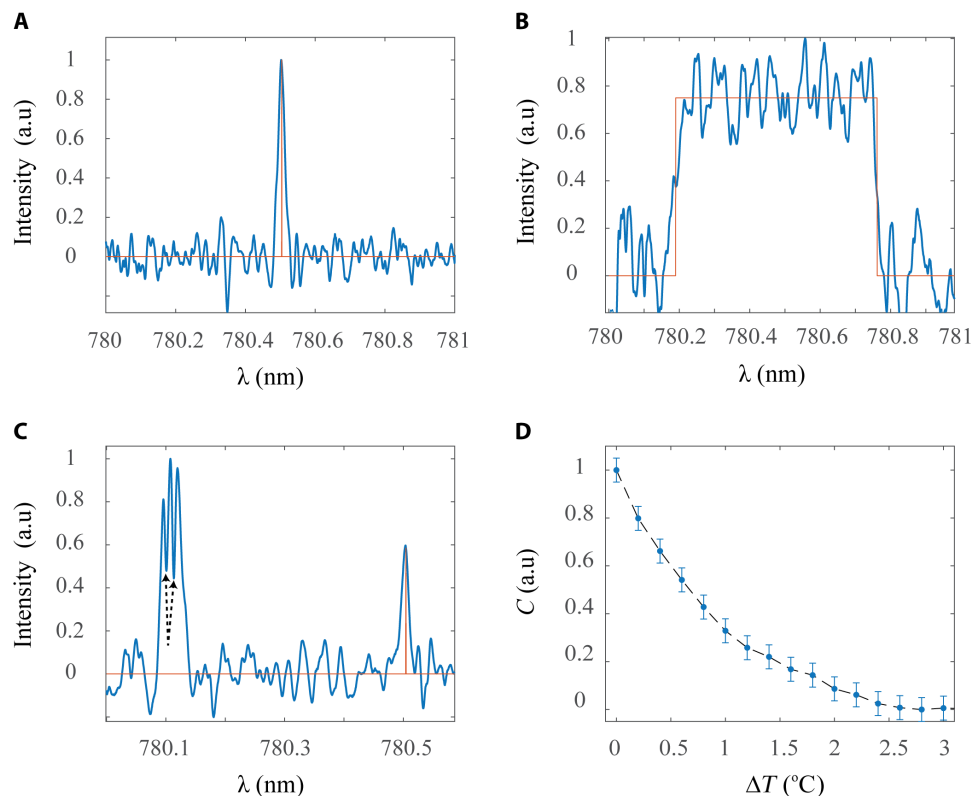
Fig. 3. Spectral reconstruction and temperature sensitivity. (**A**) Spectral reconstruction of a single frequency using the truncated SVD algorithm (blue) compared to the true input (red). (**B**) Reconstruction of a broad uniform spectrum (blue) compared to the true input (red). (**C**) Spectral reconstruction of a single frequency together with a broad source encompassing the Rb D$_2$ absorption region (blue) compared to the true input of the single wavelength (red). The absorption lines are marked with black arrows. (**D**) Correlation values as a function of temperature. The blue dots correspond to the correlation extracted from the measured data, and the trend line is given by the dashed line.

(as in most practical scenarios), the reconstruction quality is severely deteriorated because of temperature fluctuations, and the wavelength cannot be retrieved. To resolve this issue, it is possible to add a temperature-stabilizing module; however, this will markedly increase the cost, size, and power consumption of the system. Therefore, here we take a different approach and implement a machine learning algorithm to provide the desired robustness against temperature fluctuations.

To gain better robustness against environmental (e.g., temperature) fluctuations, we implemented a k-neighbor classification algorithm (kNN). To do so, many scans of the laser are performed while the temperature naturally fluctuates over time. All these scans are used as a training set for the kNN algorithm: For each new inspected source (i.e., measurement of unknown wavelength, in unobserved temperature), we use our entire training set to look for the best match for this measured output. The best match represents a training scan that contains a frequency measurement similar to our new output pattern, among all the possible scans. We use a cross-validation scheme to empirically test our method (the process is implemented using the algorithm KNeighborsClassifier from the Faiss Python package; see Materials and Methods).

First, in Fig. 4A, we show a comparison of a single wavelength reconstruction for both SVD (blue) and kNN (black) algorithms under stable environmental conditions and using the best matching training scan. Even when both algorithms provide excellent spectrum reconstruction, the kNN approach exhibits a twofold higher

spectral resolution, i.e., peak width of ~0.01 nm at FWHM and a 10-fold better signal-to-noise ratio (SNR) (evaluated as the one divided by SD of the noise). In contrast, Fig. 4B shows the spectrum reconstruction when a considerable time has elapsed between the transmission matrix acquisition and the interrogation of the unknown source using both algorithms. The advantage of the kNN algorithm (black) over the simple linear SVD approach (blue) in this case is vividly observed. Beyond a demonstration of a single-spectrum reconstruction, we further analyzed the degradation in performances of the device over time for both algorithms by considering the accuracy to which the unknown wavelength was determined over a time period of ~30 min. Figure 4C presents the deviation from the ground truth for increasing differences between scans; clearly, the kNN algorithm (black) maintains a superior accuracy over time because of the robustness against thermal fluctuations. We note that by using for each measurement its best-adjusted scans from the training set and fitting the data to determine the accurate location of a single peak, the resolution can approach the value of ~0.001 nm (using the SVD method) or ~0.0005 nm (using the kNN method).

DISCUSSION
The miniaturization of optical spectrometers is rapidly advancing toward the holy grail of supporting integrated applications (*15, 17–24*). Spatial to spectral mapping is a natural very effective choice, which comes at the cost of a trade-off between size and spectral resolution.
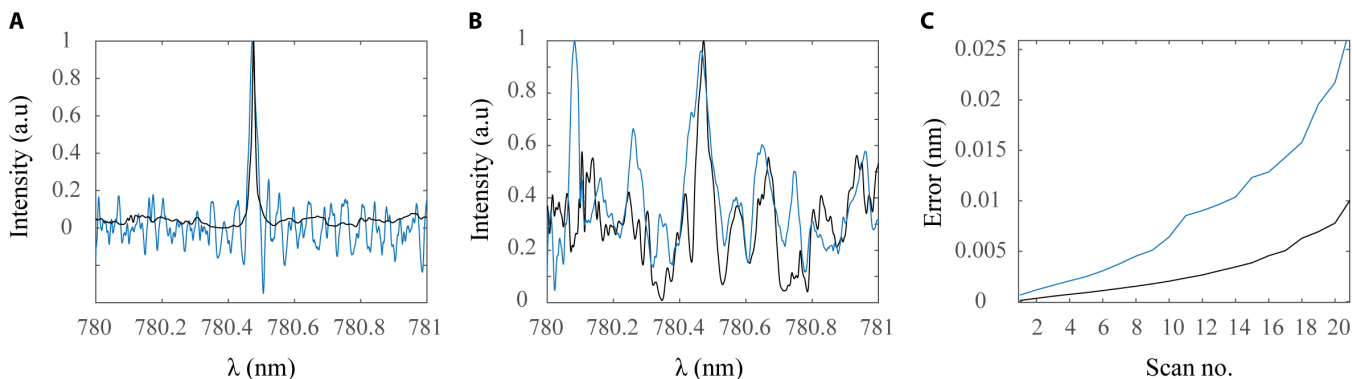
Fig. 4. Machine learning spectral reconstruction. (**A**) Spectral reconstruction of a single frequency at stable environmental conditions using the truncated SVD algorithm (blue) and a kNN algorithm (black). (**B**) Same as (A) with ~30-min time delay between the transmission matrix and the single wavelength measurements. (**C**) Accuracy of the kNN (black) and SVD (blue) algorithms for many measurements taken at increasing time delays.

The introduction of random media with a large number of degrees of freedom together with a suitable reconstruction algorithm markedly reduced the size requirement and supports high spectral resolution (up to 0.01 nm). Yet, the added sensitivity renders the system susceptible to thermal fluctuations. Furthermore, calibration with an external source is needed to provide absolute value of accuracy rather than relative value of precision. Here, we presented a novel approach in which a chip-scale multimode waveguide is encapsulated within an Rb vapor cell on the chip and is combined with a classification machine learning algorithm to provide robustness against environmental fluctuations. The photonic chip provides miniaturization, whereas the Rb vapor enables internal calibration, and the machine learning algorithm is shown to be useful in providing robustness against environmental (e.g., thermal) fluctuations. Machine learning approaches have been recently introduced to advance various aspects of photonic-based capabilities such as imaging and manipulation of electromagnetic radiation (25, 26). Following this route, here we have demonstrated a new implementation particularly suitable for spectral analysis. The nonlinear kNN algorithm has shown outperforming results both in relatively close training scans and ones of substantially different temperatures. We note that as the kNN is a nonlinear algorithm, its response to a combination of inputs in different frequencies is more complicated than that of the SVD linear response. In cases where one aims to detect a combination of frequencies, we advise using sparse coding algorithms (27) to better cope with mixed signals without suffering the spread of the signal following the use of the SVD method.

Compared to other miniaturized spectrometers, our device presents a higher spectral resolution than merely all other modalities [see Figure 6a in (15)] and can operate within the entire optical range for which silicon nitride is transparent (i.e., ~300 to 7000 nm). Moreover, beyond the classification algorithm, the naturally low thermo-optical coefficient of silicon nitride compared to silicon devices such as used in (1) further facilitates the robustness against thermal fluctuations. Yet, in terms of total footprint, the radius of our spiral device is larger than in (1); however, this is merely a matter of balancing the trade-offs between three different system parameters depending on one's prioritization: bandwidth, spectral window of operation, and throughput. Compared to (1), the 50-μm width of our multimode waveguide can facilitate a larger bandwidth but enforces a fivefold increase in the spiral radius. The refractive index of silicon nitride is almost half that of silicon, which enforces a longer propagation distance in our work, yet it enables measurements over a large spectral window including the visible and the infrared regime. Last, we have not implemented an "evanescently coupling" mechanism as it introduces a significant amount of loss and degrades the throughput by more than an order of magnitude (see the Supplementary Materials).

The presence of Rb atoms within the vicinity of the waveguide is a unique feature of our design. To claim an absolute spectral resolution in the order of 10 pm, the calibration matrix (i.e., the transmission matrix in Fig. 2B) needs to be constructed with at least the same accuracy. Hence, when the laser is scanned over the range of interest to generate such matrix, the starting point as well as the scanning speed need to be known to a very high precision (better than the claimed spectral resolution). This can be achieved using external equipment such as high-end wave-meters to tune the exact scanning parameters; however, this adds complexity and expenses to the system, while the integrated Rb cell provides an elegant compact and very accurate alternative. Moreover, a broadband source encompassing the Rb absorption region can be injected into the device together with the source of interest to provide an absolute measurement of the wavelength as we have shown in Fig. 3C. We note that even when a broad spectrum is reconstructed that also encompasses the Rb absorption region, it will not interfere with the ability to visualize the absorption lines of the Rb because of their very sharp absorption features relative to the noise variations. Moreover, the absorption contrast of the Rb lines can be further improved, e.g., by increasing the vapor-cell temperature and, as a result, also the atomic vapor density. Beyond the ability to accurately calibrate the system (i.e., ensure that each wavelength scan is performed over the exact spectral band), it can also facilitate a variety of capabilities. For instance, the absorption contrast can serve as a precise thermometer. Moreover, the output can be used to lock the frequency of a laser within a miniaturized architecture (8, 28, 29).

MATERIALS AND METHODS
Fabrication
We used a 500-μm-thick silicon wafer covered with a 2-μm oxide layer and a 250-nm CVD Si_3N_4 layer. We coated the wafer with a diluted (3:1) ZEP520 to serve as an electron beam resist and transferred the

desired pattern defined using an online lithography toolbox (*30*) via e-beam lithography (Elionix); the exposed regions were removed after development. Next, we etched the sample by reactive ion etching (RIE) (Corial 210-RL), leaving the top and side boarders of the waveguide exposed to air. We then deposited a 2-μm-thick layer of oxide on top of the entire device to ensure uniform cladding and to isolate the waveguide from the surrounding environment. To allow for interactions between the Rb atoms and the spiral waveguide, it was necessary to expose the regions of interest within the device to the surrounding. Hence, we carried out a second lithography process in which a large circular feature was patterned inside the spiral region, and the oxide under the pattern was removed via buffer HF immersion. Next, the exit port of the device was diced, leaving an exposed cross section of the waveguide to be imaged. Last, the device was encapsulated within a glass chamber, and rubidium was inserted as described elsewhere. (*28*)

Algorithm implementation
For SVD implementation, we followed the general approach outlined in (*13*). The measured transmission matrix was decomposed by applying the SVD command in MATLAB or NumPy in Python. Next, the obtained diagonal matrix "S" was truncated by setting a threshold. The optimal threshold value set by maximizing the SNR of the results was found to be ~0.008, which yielded an SNR value of ~18.

The alternative classification algorithm was evaluated by the following steps: After obtaining many transmission matrices by performing many scans, each matrix at a time was chosen as test data, while the remaining matrices were used as the training scans (this process is equivalent to the evaluation SVD approach). Next, the training data are labeled with a spectral resolution according to the corresponding frequency bandwidth. The test data are classified, using the best-fitted train signal from each scan ($k = 1$), and the difference between the known wavelengths and those predicted by the algorithm determines the accuracy of that scan.

REFERENCES AND NOTES
1. B. Redding, S. Fatt Liew, Y. Bromberg, R. Sarma, H. Cao, Evanescently coupled multimode spiral spectrometer. *Optica* **3**, 956–962 (2016).
2. G. Scarcelli, S. H. Yun, Confocal Brillouin microscopy for three-dimensional mechanical imaging. *Nat. Photonics.* **2**, 39–43 (2008).
3. E. Edrei, M. Nikolic, G. Scarcelli, Improving localization precision of Brillouin measurements using spectral autocorrelation analysis. *J. Innov. Opt. Health Sci.* **10**, 1742004 (2017).
4. B. Mollow, Power spectrum of light scattered by two-level systems. *Phys. Rev.* **188**, 1969–1975 (1969).
5. J. Sandercock, Brillouin scattering study of SbSI using a double-passed, stabilised scanning interferometer. *Opt. Commun.* **2**, 73–76 (1970).
6. L. Couturier, I. Nosske, F. Hu, C. Tan, C. Qiao, Y. H. Jiang, P. Chen, M. Weidemüller, Laser frequency stabilization using a commercial wavelength meter. *Rev. Sci. Instrum.* **89**, 043103 (2018).
7. S. Kobtsev, S. Kandrushin, A. Potekhin, Long-term frequency stabilization of a continuous-wave tunable laser with the help of a precision wavelength meter. *Appl. Optics* **46**, 5840–5843 (2007).
8. R. Zektzer, M. T. Hummon, L. Stern, Y. Sebbag, Y. Barash, N. Mazurski, J. Kitching, U. Levy, a chip-scale optical frequency reference for the telecommunication band based on acetylene. *Laser Photonics Rev.* **14**, 1900414 (2020).
9. E. Edrei, G. Scarcelli, Brillouin microspectroscopy through aberrations via sensorless adaptive optics. *Appl. Phys. Lett.* **112**, 163701 (2018).
10. H. Cao, Perspective on speckle spectrometers. *J. Opt.* **19**, 060402 (2017).
11. N. K. Metzger, R. Spesyvtsev, G. D. Bruce, B. Miller, G. T. Maker, G. Malcolm, M. Mazilu, K. Dholakia, Harnessing speckle for a sub-femtometre resolved broadband wavemeter and laser stabilization. *Nat. Commun.* **8**, 15610 (2017).
12. B. Redding, H. Cao, Using a multimode fiber as a high-resolution, low-loss spectrometer. *Opt. Lett.* **37**, 3384–3386 (2012).
13. B. Redding, S. M. Popoff, H. Cao, All-fiber spectrometer based on speckle pattern reconstruction. *Opt. Express* **21**, 6584–6600 (2013).
14. B. Redding, S. F. Liew, R. Sarma, H. Cao, Compact spectrometer based on a disordered photonic chip. *Nat. Photonics* **7**, 746–751 (2013).
15. Z. Yang, T. Albrow-Owen, W. Cai, T. Hasan, Miniaturization of optical spectrometers. *Science* **371**, (2021).
16. A. Arbabi, L. L. Goddard, Measurements of the refractive indices and thermo-optic coefficients of Si₃N₄ and SiOx using microring resonances. *Opt. Lett.* **38**, 3878–3881 (2013).
17. Z. Yang, T. Albrow-Owen, H. Cui, J. Alexander-Webber, F. Gu, X. Wang, T. C. Wu, M. Zhuge, C. Williams, P. Wang, A. V. Zayats, W. Cai, L. Dai, S. Hofmann, M. Overend, L. Tong, Q. Yang, Z. Sun, T. Hasan, Single-nanowire spectrometers. *Science* **365**, 1017–1020 (2019).
18. M. Faraji-Dana, E. Arbabi, A. Arbabi, S. M. Kamali, H. Kwon, A. Faraon, Compact folded metasurface spectrometer. *Nat. Commun.* **9**, 1–8 (2018).
19. J. Meng, J. J. Cadusch, K. B. Crozier, Detector-only spectrometer based on structurally colored silicon nanowires and a reconstruction algorithm. *Nano Lett.* **20**, 320–328 (2020).
20. Z. Wang, S. Yi, A. Chen, M. Zhou, T. S. Luk, A. James, J. Nogan, W. Ross, G. Joe, A. Shahsafi, K. X. Wang, M. A. Kats, Z. Yu, Single-shot on-chip spectral sensors based on photonic crystal slabs. *Nat. Commun.* **10**, 1–6 (2019).
21. Y. M. Eltagoury, Y. M. Sabry, D. A. Khalil, All-silicon double-cavity fourier-transform infrared spectrometer on-chip. *Adv. Mater. Technol.* **4**, 1900441 (2019).
22. R. F. Wolffenbuttel, MEMS-based optical mini- and microspectrometers for the visible and infrared spectral range. *J. Micromech. Microeng.* **15**, S145–S152 (2005).
23. R. DeCorby, N. Ponnampalam, E. Epp, T. Allen, J. McMullin, Chip-scale spectrometry based on tapered hollow Bragg waveguides. *Opt. Express* **17**, 16632–16645 (2009).
24. A. Li, Y. Fainman, On-chip spectrometers using stratified waveguide filters. *Nat. Commun.* **12**, 1–9 (2021).
25. L. Li, H. Ruan, C. Liu, Y. Li, Y. Shuang, A. Alù, C. W. Qiu, T. J. Cui, Machine-learning reprogrammable metasurface imager. *Nat. Commun.* **10**, 1–8 (2019).
26. R. Zhu, T. Qiu, J. Wang, S. Sui, C. Hao, T. Liu, Y. Li, M. Feng, A. Zhang, C. W. Qiu, S. Qu, Phase-to-pattern inverse design paradigm for fast realization of functional metasurfaces via transfer learning. *Nat. Commun.* **12**, 1–10 (2021).
27. M. Aharon, M. Elad, A. Bruckstein, K-SVD: An algorithm for designing overcomplete dictionaries for sparse representation. *IEEE Trans. signal processing.* **54**, 4311–4322 (2006).
28. L. Stern, B. Desiatov, I. Goykhman, U. Levy, Nanoscale light-matter interactions in atomic cladding waveguides. *Nat. Commun.* **4**, 1548 (2013).
29. R. Zektzer, N. Mazurski, Y. Barash, Nanoscale atomic suspended waveguides for improved vapour coherence times and optical frequency referencing. *Nat. Photonics* **15**, 772–779 (2021).
30. K. C. Balram, D. Westly, M. I. Davanco, K. E. Grutter, Q. Li, T. Michels, C. H. Ray, R. Kasica, C. B. Wallin, I. J. Gilbert, B. A. Bryce, G. Simelgor, J. Topolancik, N. Lobontiu, Y. Liu, P. Neuzil, V. Svatos, K. A. Dill, N. A. Bertrand, M. Metzler, G. Lopez, D. Czaplewski, L. Ocola, K. Srinivasan, S. Stavis, V. Aksyuk, J. A. Liddle, S. Krylov, R. Ilic, The nanolithography toolbox. *J. Res. Natl. Inst. Stand.* **121**, 464–475 (2016).